Hydrothermal synthesis, crystal structure, and vibrational and Mössbauer spectra of a new tricationic orthophosphate — $KCo_3Fe(PO_4)_3$[1]

Hassane Assaaoudi, Zhen Fang, Dominic H. Ryan, Ian S. Butler, and Janusz A. Kozinski

Abstract: Crystals of a new potassium cobalt(II) iron(II) triorthophosphate salt, $KCo_3Fe(PO_4)_3$, as well as amorphous nanoparticles of the same material have been produced by hydrothermal reactions, under supercritical water (SCW) conditions, of equivalent quantities of aq. $CoCl_2 \cdot 6H_2O$ (2 mol/L) and $K_4P_2O_7$ (1 mol/L) in concd. HCl in a stainless steel batch reactor at 400–450 °C and 25–32 MPa. The dark-violet crystals of the new salt have been characterized by single-crystal X-ray diffraction and IR, Raman, and Mössbauer spectroscopy. The Fe(II) in the new orthophosphate salt must derive from leaching of iron from the stainless steel walls of the reactor by concd. HCl under the SCW conditions. The salt crystallizes in the orthorhombic space group *Pnnm*, $Z = 4$, with unit cell parameters as follows: $a = 9.672(1)$ Å, $b = 16.457(2)$ Å, $c = 6.2004(8)$ Å, $V = 986.97$ Å^3. Microporous $KCo_3Fe(PO_4)_3$ exhibits infinite chains of corner-sharing [PO_4^{3-}], [FeO_6], and [CoO_5] units, which form two large rhombus tunnels, occupied by K^+ ions, running parallel to [100] in the unit cell. The vibrational spectra have been interpreted partly on the basis of factor group effects and are in accord with the centrosymmetric structure of the material. The particle sizes of this new nanomaterial and their distribution have been determined by scanning electron micrography and laser scattering particle size distribution analysis, while the amorphous nanomaterial has also been characterized by X-ray powder diffraction and Raman spectroscopy.

Key words: crystal structure, vibrational and Mössbauer spectra, orthophosphate, nanomaterial.

Résumé : Les cristaux du nouveau sel tri-orthophosphate de potassium, cobalt(II) et fer(II), $KCo_3Fe(PO_4)_3$, ainsi que des nano particules amorphe du même matériel, ont été produites par réactions hydrothermal dans des conditions supercritique de l'eau. Ils sont obtenus à partir d'un mélange équimolaire des solutions aqueuses $CoCl_2 \cdot 6H_2O$ (2 mol/L), et $K_4P_2O_7$ (1 mol/L), en milieu acide HCl concentré dans un tube en acier inoxydable à températures 400–450 °C, et à pression 25–32 MPa. Les cristaux violets foncés du nouveau sel ont été caractérisés par diffraction des rayons-X sur monocristal, et par spectroscopie IR, Raman et Mössbauer. Le Fe(II) du nouveau sel d'orthophosphate provient d'une infiltration à partir de la parois interne du réacteur en acier inoxydable, sous l'effet de l'acide HCl concentré dans les conditions supercritique de l'eau. Le sel cristallise dans le système orthorhombique de groupe d'espace *Pnnm*, avec $Z = 4$. Les paramètres cristallographiques de la maille sont : $a = 9.672(1)$ Å, $b = 16.457(2)$ Å, $c = 6.2004(8)$ Å, $V = 986.97$ Å^3. La structure microporeuse de $KCo_3Fe(PO_4)_3$ se présente sous forme de chaînes formées des groupements [PO_4^{3-}], [CoO_5] et [FeO_6]. Ils partageant des atomes en commun, créant ainsi deux larges tunnels par maille élémentaire. Ils sont alignés le long de l'axe [100], en forme rhomboèdre, logés par des cations K^+. Les spectres de vibration ont été interprétés en utilisant l'analyse du groupe facteur des groupements PO_4^{3-}. L'absence de coïncidence entre la plupart des fréquences de vibrations IR et Raman est en accord avec la structure centro-symétrique du matériau. La taille et la répartition des nouvelles nanoparticules amorphes ont été déterminées par la micrographie SEM, et l'analyseur de distribution de taille des particules par diffusion laser. Ce matériau est caractérisé par diffraction des rayons-X sur poudre et par spectroscopie Raman.

Mots clés : structure cristalline, spectres de vibration et Mössbauer, orthophosphate, nanomatériau.

Received 1 March 2005. Published on the NRC Research Press Web site at http://canjchem.nrc.ca on 22 February 2006.

H. Assaaoudi. Department of Chemistry, Otto Maass Building, McGill University, 801 Sherbrooke Street West, Montreal, QC H3A 2K6, Canada and Energy and Environmental Research Group, Department of Mining, Metals and Materials Engineering, Wong Building, Room 2290, McGill University, 3610 University St., Montreal, QC H3A 2B2, Canada.
I.S. Butler.[2] Department of Chemistry, Otto Maass Building, McGill University, 801 Sherbrooke Street West, Montreal, QC H3A 2K6, Canada.
Z. Fang and J.A. Kozinski. Energy and Environmental Research Group, Department of Mining, Metals and Materials Engineering, Wong Building, Room 2290, McGill University, 3610 University St., Montreal, QC H3A 2B2, Canada.
D.H. Ryan. Department of Physics and Centre for the Physics of Materials, 3600 University St., McGill University, Montreal, QC H3A 2T8, Canada.

[1]This article is part of a Special Issue dedicated to Professor Arthur Carty.
[2]Corresponding author (e-mail: ian.butler@mcgill.ca).

 doi:10.1139/V05-235 © 2006 NRC Canada

Fig. 1. Evolution of products obtained from reaction under SCW conditions (450 °C, 32 MPa, and vol(HCl):vol(Co) = 2:5) after 5, 30, 60, and 120 min.

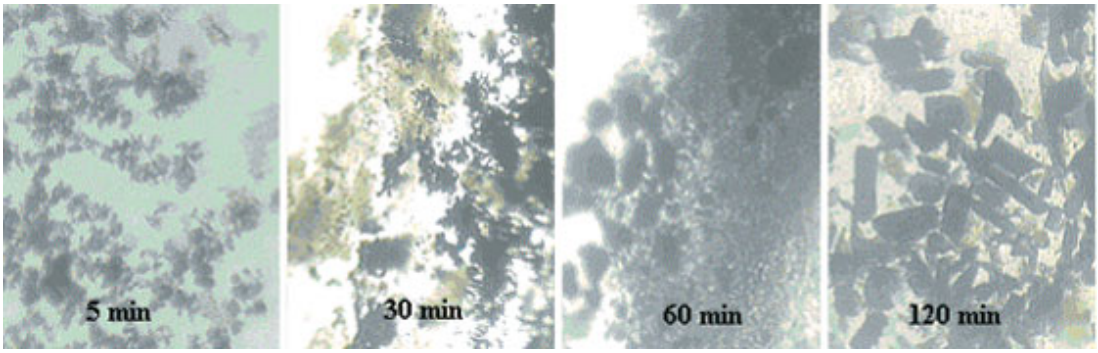

Introduction

Hydrothermal synthesis has been carried out since the end of the 19th century, mainly in the production of synthetic minerals to imitate natural geothermal processes (1, 2). More recently, both near-critical and supercritical water (SCW) have been used as reaction media for the synthesis of highly crystalline metal oxides (2–5). The use of the SCW approach has only just been demonstrated for phosphate materials in the formation of highly crystalline, micro-sized particles of $LiFePO_4$ (6). Numerous orthophosphates built from discrete PO_4^{3-} tetrahedra (7) have been characterized over the past 20 years, prompted by the discovery of the vast structural variety in aluminum, beryllium, and zinc phosphates. Some new potassium–iron and potassium–cobalt triorthophosphates have also been described, e.g., $KCo_4(PO_4)_3$ (8), $KFe_4(PO_4)_3$ (9), and $K_3Fe_2(PO_4)_3$ (10), and can be obtained from molten mixtures of Co(II) or Fe(II) sulfates or oxides and KBr or KCl in the presence of potassium hydrogen phosphate, at 350 °C and 1000 atm (1 atm = 101.325 kPa). Several cobalt and iron phosphates with similarities to open mineral-type frameworks have also been reported (11, 12).

The design, synthesis, and characterization of new micro- and nano-porous materials, such as polyphosphates, is of enormous interest because of the many potential industrial applications, e.g., heterogeneous catalysis, gas absorption, and ion exchange. Micro- and nano-porous catalysts often display high selectivity because the channel apertures may allow only certain reactants to access the catalytically active interior of the material and only certain products to leave (13, 14). Transition-state selectivity may also be related to the position and degree of substitution of catalytically active sites in the framework structure, where the active site can be a transition metal that might function by selective oxidation, e.g., Fe(II) and Co(II) (15). Further knowledge of the mechanism by which transition metals substitute into the framework structures of porous materials is, therefore, of considerable importance, both for controlling the number of catalytically active sites in such materials and also for fine tuning their function by manipulating the specific positions and coordination environments of the active centers (16).

In this paper, we present analytical, structural, and spectroscopic data for a new crystalline, open framework, tricationic orthophosphate salt, $KCo_3Fe(PO_4)_3$, and amorphous nanoparticles of the same material produced under SCW conditions. The effects of temperature, pH, and reaction time on the size and size distribution of the particles have also been investigated.

Experimental section

Synthesis

Crystals of $KCo_3Fe(PO_4)_3$, as well as nanoparticles of the same material, were obtained from the reaction between equivalent amounts of aqueous cobalt $CoCl_2{\cdot}6H_2O$ (2 mol/L) and $K_4P_2O_7$ (1 mol/L) in a predetermined volume of concd. HCl (35%), (vol(HCl):vol(Co) = 2:5 or 3:5). The final red solution obtained was transferred quickly to a stainless steel batch reactor (volume = 6 mL; length = 105 mm, o.d. = 12.7 mm (1/2 in)). Both temperature and pressure were measured with a pressure transducer fitted with a J-type thermocouple (Dynisco E242). The pressure was also calculated by first calculating the density of water ((weight of water added)/(volume of batch reactor) ≈ 1.6 g/mL), assuming that only water contributed to the pressure. Bassett et al. (17) have compared the pressures obtained by such calculations with the *P–T* boundary of the α–β transition in quartz and have shown that the pressure difference is less than 4% between the two methods. Approximately 1 mL of the final solution was loaded into the reactor, which, after being sealed and connected to a data acquisition system, was submerged in a fluidized sand bath (Omega FSB- 3) or placed into a tubular furnace. The reactor was heated at a rate of 3.5 °C/s to 400–450 °C and then held at this temperature for 5, 10, 30, 60, or 120 min. After each given period, the reactor was quenched in cold water, and the reaction mixture was emptied into a flask. The reactor was washed with water, and the washings were added to the same flask. The solution in the flask was filtered through a membrane filter to yield a solid phase, which was dried at room temperature. Well-shaped, dark-violet crystals (Fig. 1) were produced under the conditions reported in Table 1. The aqueous phase was left at room temperature for about 1 to 2 h, after which a grey-violet powder appeared, which was subsequently filtered and analyzed (Table 1).

© 2006 NRC Canada

Table 1. Experimental conditions and results.

	Run				
	1	2	3	4	5
HCl (mol/L)	0.6	0.6	0.6	0.4	0.4
T (°C)	25	400	450	400	450
P (MPa)	0.1	25	32	25	32
Products					
0 min	—	—	—	—	—
5 min	—	P	P	P	P
10 min	—	P	P	P	P
30 min	—	P	P	P	P
60 min	$Co_2P_2O_7{\cdot}6H_2O$[a]	P	$KCo_3Fe(PO_4)_3$	$KCo_3Fe(PO_4)_3$	$KCo_3Fe(PO_4)$
120 min	$Co_2P_2O_7{\cdot}6H_2O$[a]	P	$KCo_3Fe(PO_4)_3$	$KCo_3Fe(PO_4)_3$	$KCo_3Fe(PO_4)$
Chemical analysis of powder P					
Co (%)	—	≈0	≈0	≈0	≈0
Fe (%)	—	15–17	25–30	14–17	25–30
P (%)	—	9–11.5	18–22	9–11	18–20
K (%)	—	2.5–5	2.5–5	2.5–5	3–5

[a]Reference 18.

Spectroscopic and crystallographic analyses

The powders obtained in the experiments were characterized by X-ray powder diffraction (XRD),[3] ICP chemical analyses, scanning electronic microscopy (SEM), and Raman spectroscopy. Crystalline $KCo_3Fe(PO_4)_3$ was analyzed by SEM and X-ray energy dispersive analysis (EDS) and was further characterized by IR, Raman, and Mössbauer spectroscopy, as well as by single-crystal X-ray diffraction.

A Philips model PW1710, vertical goniometer, X-ray powder diffractometer with a Cu Kα radiation source was used for the powder diffraction measurements. The samples were scanned over the range from 5° or 10° to 60° at a step size (2θ) of 0.02° and a measurement time of 0.5 s/step. Chemical analyses were performed using ICP-AES on a Thermo Jarrell Ash TraceScan axial torch sequential ICP system. The morphology of the particles was investigated using a field emission SEM (model JSM-840), while EDS (model EDAX) was used to characterize the materials (powder and crystals). The size distribution of the particles was determined using a laser scattering particle size distribution analyzer (model Horiba LA-920), which can measure particle size distributions over a wide range of sizes — from 0.02 to 2000 μm — in dry or slurry form.

Infrared spectra were recorded at ambient temperature on a Bomem MB100 FT-IR spectrometer at 2 cm^{-1} resolution (50 scans), using the KBr pellet technique. The wavenumber accuracy is considered to be within ±1 cm^{-1} for sharp bands. Raman spectra were measured on a Renishaw 3000 Raman microscope (20× objective), using the 514.5 nm line of an Ar^+-ion laser for excitation (5–100 mW laser power; 1 cm^{-1} spectral slit width; 5 s exposure time; 10 accumulations). The band positions are considered to be accurate to at least ±1 cm^{-1}. The Mössbauer effect measurements were made at room temperature with a Wissel spectrometer. The spectra were recorded using the radiation from ^{57}Co in Rh with a 512 multichannel analyzer. The velocity was calibrated using iron metal as a standard.

A summary of the X-ray data collection and refinement is given in Table 2. A Bruker D8 Discover diffractometer was used for examination of the crystal. The structure was solved by direct methods using SHELXS97 (19) and was refined by a full-matrix, least-squares technique, SHELXL97 (20). The molecular drawings obtained with ORTEP III (21) were manipulated using the WINGX system of programs (22) and the program Molview (23). The X-ray data resulted in the formula $KCo_3Fe(PO_4)_3$ for the compound after checking the final residuals R, R_w ($I > 2\sigma(I_{obs})$), and GOF for different ratios of Co and Fe atoms and taking anisotropic thermal parameters into account.

Results

Identification of materials

The XRD patterns of the powders obtained from the SCW reactions under the conditions reported in Table 1 showed that the materials were amorphous. The Fe, Co, K, and P analyses of these powders were performed using ICP-AES. The results obtained correspond to the composition shown in Table 1. The morphology of the particles and the distribution of their sizes were determined by SEM (Fig. 2*a*). The composition of crystalline $KCo_3Fe(PO_4)_3$ and the powder were determined using EDS analysis, and the results showed that their compositions were essentially identical except for the amount of Co present (Figs. 2*b* and 2*c*) because, irrespective

[3] Supplementary data for this article are available on the journal Web site (http://canjchem.nrc.ca) or may be purchased from the Depository of Unpublished Data, Document Delivery, CISTI, National Research Council Canada, Ottawa, ON K1A 0R6, Canada. DUD 4080. For more information on obtaining material refer to http://cisti-icist.nrc-cnrc.gc.ca/irm/unpub_e.shtml. CCDC 415778 contains the crystallographic data for this manuscript. These data can be obtained, free of charge, via www.ccdc.cam.ac.uk/conts/retrieving.html (Or from the Cambridge Crystallographic Data Centre, 12 Union Road, Cambridge CB2 1EZ, UK; fax +44 1223 336033; or deposit@ccdc.cam.ac.uk).

© 2006 NRC Canada

Table 2. Crystal data and structure refinement for KCo_3FePO_4.

Crystal data	
Formula	$KCo_3FeO_{12}P_3$
MW	556.66
V (Å^3)	987.0(2)
Z	4
Colour, habit	Dark violet, block
Crystal dimensions (mm^3)	0.10 × 0.10 × 0.10
D_x (Mg m^{-3})	3.746
Crystal system	Orthorhombic
Space group	*Pnnm* (No. 58)
a (Å)	9.6722(12)
b (Å)	16.457(2)
c (Å)	6.2004(8)
T (K)	153(2)
μ (mm^{-1})	4.221
Radiation	Mo Kα
l (Å)	0.710 73
Data collection	
Instrument	Bruker D8 Discover
Scans	w-2q
Reflections collected	4619
Independent reflections	1074 ($R_{(int)}$ = 0.1028)
q_{max}	26.73
Collection ranges	$-11 \le h \le 7$; $-19 \le k \le 20$; $-7 \le l \le 7$
R_{int}	0.1028
Refinement	
Refinement	On F^2
R ($F^2 > 2s(F^2)$)	0.0339
R (F^2, all data)	0.0356
wR (F^2)	0.0924
Dr_{max} (e Å^{-3})	1.171
Dr_{min} (e Å^{-3})	–0.945
Parameters	104

of the SCW experimental conditions employed, the powders obtained did not contain any Co. The carbon peak in Figs. 2*b* and 2*c* is associated with the agent used to immobilize the particles for analysis. The powder nanoparticles are spherical, and the particle size ranges from 100 to 800 nm, with an average size of about 500 nm (Fig. 2*a*).

Iron(III) has five electrons in the 3d valence subshell, which makes it spherically symmetric, thereby practically eliminating any electric field gradient and quadrupole splitting (QS). On the other hand, Fe(II) has one extra electron in the 3d valence subshell, thus introducing an asymmetry resulting in an electric field gradient and a detectable QS. From the Mössbauer effect measurements undertaken in this work (Fig. 3), the values obtained for both the isomer shift (IS) and the QS for the iron atoms present in the new orthophosphate material are typical of Fe(II) (24). The expected Fe(II) doublet is observed with IS = 1.2 and QS = 2.9 mm/s. This definitive demonstration of the presence of Fe(II) means that the cobalt atoms in $KCo_3Fe(PO_4)_3$ must be in the Co(II) state to charge compensate for the three PO_4^{3-} ions. The Fe(II) ions must have been produced by iron being leached from the stainless steel walls of the reactor by concd. HCl under the SCW conditions employed.

Effect of synthesis temperature

Two temperatures under SCW conditions (400 and 450 °C) were investigated. From the quantity of crystals obtained at these two different temperatures, the production of crystalline $KCo_3Fe(PO_4)_3$ was much more favorable at 450 °C than at 400 °C. The particles produced at 450 °C (with all the other conditions being kept constant) have a slightly narrower size distribution than do those obtained at 400 °C (Fig. 4*a*). This figure also shows that the particles decrease in size with increasing temperature, although the size distribution is quite broad.

Effect of pH

The effect of pH was investigated by adjusting the amount of HCl added. The reaction between equivalent quantities of aqueous cobalt $CoCl_2{\cdot}6H_2O$ (2 mol/L) and $K_4P_2O_7$ (1 mol/L) was limited by the amount of concd. HCl that could be added while avoiding instantaneous precipitation from solution and yet still permitting synthesis of $KCo_3Fe(PO_4)_3$ crystals under SCW conditions (vol(HCl):vol(Co) = 2:5 and 3:5). The particles synthesized at a vol(HCl):vol(Co) ratio of 3:5 tended to exhibit a narrower size distribution than did those obtained for a vol(HCl):vol(Co) ratio of 2:5. The particles had an average size range of 100 μm to submicron (Fig. 4*b*). Compared to the influence of other parameters on the particle sizes produced under SCW conditions and their distribution, the effect of pH was by far the most important.

Effect of residence time

The influence of residence time (τ) in the reactor was investigated by carrying out hydrothermal reactions at 400 °C with τ = 0, 5, 10, 30, 60, and 120 min. The vol(HCl):vol(Co) ratio was maintained at 3:5 to keep the pH of the reactant mixture constant. No significant difference in morphology was observed with changing residence time. The particles produced when τ = 120 min, however, had a narrower size distribution than did those obtained after 10 min (Fig. 4*c*). Similar results were obtained when the reaction temperature was 450 °C, with all other conditions being kept constant.

Crystal structure

The structure of the new orthophosphate is built up from [FeO_6] octahedra, [CoO_5] pentahedra, [KO_8] heptahedra, and [PO_4^{3-}] tetrahedra sharing corners and edges to form a 3-D open framework (Fig. 5). There are three crystallographically distinct P atoms, all with tetrahedral coordination, and two distinct Co atoms. The Co(2), O(3), O(4), and O(7) atoms occupy general positions. All the other atoms occupy special positions on mirror plane symmetry. Atomic coordinates and isotropic thermal parameters are given in Table 3 and selected interatomic distances in Table 4. The Co atoms are arranged in five-vertex polyhedra, like distorted square-based pyramids for both the Co(1) and Co(2) atoms. Their average bond distances are Co(1)—O_{av} = 2.056 Å and Co(2)—O_{av} = 2.084 Å; the Co atoms are surrounded by O atoms from four and five different phosphate anions, respec-

© 2006 NRC Canada

Fig. 2. (*a*) Scanning electron micrographs of powder obtained after reaction at 400 °C, 120 min; (*b*) EDS analysis of powder obtained after reaction at SCW; and (*c*) EDS analysis of crystalline $KCo_3Fe(PO_4)_3$.

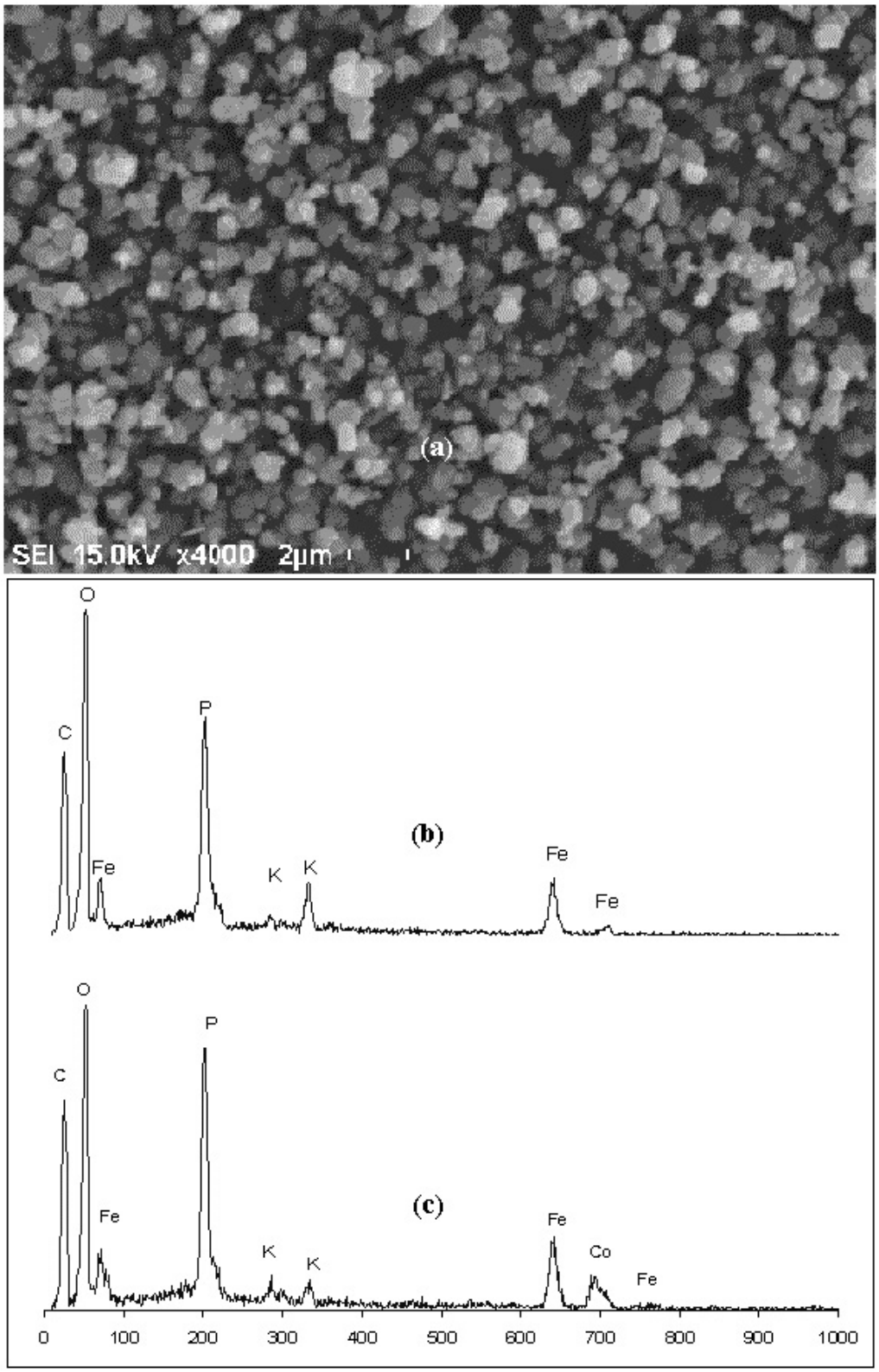

© 2006 NRC Canada

Fig. 3. Room-temperature ^{57}Fe Mössbauer spectrum of crystalline $KCo_3Fe(PO_4)_3$.

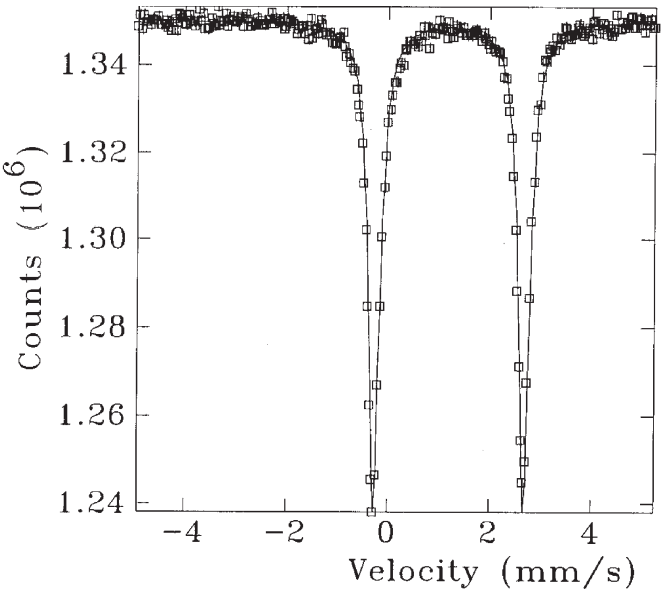

Table 3. Atomic coordinates (×10^4) and equivalent isotropic displacement parameters (Å^2 × 10^3) for $KCo_3Fe(PO_4)_3$.

Atom	Site	*x*	*y*	*z*	U_{eq}[a]
Co(1)	4g	5360(1)	4064(1)	0	4(1)
Co(2)	8h	2508(1)	2964(1)	–2515(1)	7(1)
Fe	4g	–179(1)	3609(1)	0	5(1)
K	4g	2948(1)	329(1)	0	12(1)
P(1)	4g	2117(2)	4621(1)	0	6(1)
P(2)	4g	4578(1)	2170(1)	0	6(1)
P(3)	4g	437(1)	1662(1)	0	5(1)
O(1)	4g	3674(4)	4777(2)	0	9(1)
O(2)	4g	–1411(4)	4563(2)	0	12(1)
O(3)	8h	1676(3)	4103(2)	1967(4)	10(1)
O(4)	8h	4016(3)	1773(2)	–2044(5)	10(1)
O(5)	4g	6167(4)	2243(2)	0	8(1)
O(6)	4g	3939(4)	3051(2)	0	8(1)
O(7)	8h	5897(3)	3787(2)	–3003(4)	8(1)
O(8)	4g	1140(4)	2530(2)	0	8(1)
O(9)	4g	3846(4)	3212(2)	–5000	8(1)

[a] U_{eq} is defined as one-third of the trace of the orthogonalized U_{ij} tensor.

tively (Table 4). The Fe coordination is tetrahedral with Fe—O in the range 1.97–2.18 Å. This tetrahedron is somewhat distorted, however, because of two additional weak Fe···O(3) and Fe···O(3)^I interactions, which are 2.316 Å in length (Table 4). Thus, the Fe coordination can be interpreted as either tetrahedral or octahedral. The latter is used in the figures for simplicity and clarity. The difference in Fe coordination observed here is similar to that in the isotype $KFe_4(PO_4)_3$ (9). The $[Co(1)O_5]$ pentahedron is more distorted than is the $[Co(2)O_5]$ one because of corner sharing via the oxygen atom O(6). But both pentahedra are less distorted than is the $[FeO_6]$ octahedron, which is involved in corner sharing via the oxygen atom O(8) and also has two weak bonds with oxygen atoms O(3) and O(3)^I. The distor-

Table 4. Selected bond distances (Å) for $KCo_3Fe(PO_4)_3$.

P(1)—O(1)	1.528(4)	P(2)—O(4)	1.526(3)
P(1)—O(2)^{XI}	1.507(4)	P(2)—O(4)^I	1.526(3)
P(1)—O(3)	1.548(3)	P(2)—O(5)	1.542(4)
P(1)—O(3)^I	1.548(3)	P(2)—O(6)	1.576(4)
<P—O>	1.5327	<P—O>	1.5327
P(3)—O(9)^{IV}	1.553(4)	Fe—O(2)	1.971(4)
P(3)—O(7)^{III}	1.509(3)	Fe—O(4)^{III}/O(4)^{IV}	2.088(3)
P(3)—O(7)^{IV}	1.509(3)	Fe—O(8)	2.187(4)
P(3)—O(8)	1.582(4)	Fe—O(3)/O(3)^I	2.316(3)
<P—O>	1.5382	<Fe—O>	2.161
Co(1)—O(7)/O(7)^I	1.980(3)	Co(2)—O(3)^I	2.068(3)
Co(1)—O(1)	2.029(4)	Co(2)—O(5)^V	2.042(2)
Co(1)—O(1)^{II}	2.113(4)	Co(2)—O(6)	2.090(3)
Co(1)—O(6)	2.176(4)	Co(2)—O(8)	2.166(3)
<Co(1)—O>	2.0556	Co(2)—O(9)	2.053(2)
K—O(2)^{VIII}/O(2)^{IX}	3.1665(10)	<Co(2)—O>	2.0838
K—O(3)^{VI}/O(3)^{VII}	2.783(3)	K—O(4)^I/O(4)	2.885(3)
<K—O>	2.8971	K—O(7)^{III}/O(7)^{IV}	2.754(3)

Note: Symmetry transformations used to generate equivalent atoms: ^{I}: *x*, *y*, –*z*; ^{II}: –*x* + 1, –*y* + 1, –*z*; ^{III}: *x* – 1/2, –*y* + 1/2, –*z* – 1/2; ^{IV}: *x* – 1/2, –*y* + 1/2, *z* + 1/2; ^{V}: *x* – 1/2, –*y* + 1/2, *z* – 1/2; ^{VI}: –*x* + 1/2, *y* – 1/2, *z* – 1/2; ^{VII}: –*x* + 1/2, *y* – 1/2, –*z* + 1/2; ^{VIII}: *x* + 1/2, –*y* + 1/2, *z* + 1/2; ^{IX}: *x* + 1/2, –*y* + 1/2, *z* – 1/2; ^{X}: –*x* + 1/2, *y* – 1/2, –*z* – 1/2; ^{XI}: –*x*, –*y* + 1, –*z*.

tion indices, $[(\text{cation-O})_{max} - (\text{cation-O})_{min}]/(\text{cation-O})_{av}$ (25), for Co(1), Co(2), and Fe are 0.095, 0.059, and 0.160, respectively. The $[Co(1)O_5]$ pentahedra share cis-edges with one $[Co(2)O_5]$ pentahedron via oxygen atom O(6), which belongs to a *P*(2) tetrahedron. The $[Co(2)O_9]$ dimer has different angles from an eclipsed conformation when viewed along the Co(1)—Co(2) axis, which confers a general site symmetry to this dimer. There are additional links at the shared corners to $[FeO_6]$ via O(8) and O(3). The structure results in alternating layers of $[Co_4O_{18}]$ units in a flat "S" form (or like "∫") and its opposite face in the *ab* plane, which is linked from those ends to two $[FeO_6]$ octahedra. The K atom is surrounded by six oxygen atoms at the vertices of a distorted trigonal prism (K—O = 2.754–2.885 Å) plus two other oxygen atoms at a distance of 3.166 Å. The K atoms involve a strong network between interlayers holding the structure together. Based on the work of Dumas et al. (26), who consider the K—O threshold bond to be 3.19 Å, the K atoms in $KCo_3Fe(PO_4)_3$ can be considered to form irregular $[KO_8]$ polyhedra (distortion index = 0.142). The K^+ ion, because of its large dimensions (ionic radii = 1.38, 1.46, and 1.51 Å for coordination numbers 6, 7, and 8, respectively (27)), forms more complex polyhedra with the distortion indices being extremely variable, ranging from 0.080 up to 0.199 (28–30). As can be seen from Fig. 6*c*, alternating Co, Fe, and P polyhedra form two large rhombus tunnels, occupied by K^+ ions, running parallel to < 100 > in a unit cell with diagonal lengths 5.49 Å (along the *c* axis) and 5.80 Å (along the *b* axis). Perpendicular to these axes, along the *c* axis, the structure presents other different tunnels with different shapes and sizes (Fig. 6*a*). In the previously reported crystal structures for iron phosphates, such as $LiFePO_4$ (31), Fe_2FPO_4 (32), $(Fe,Zn)_3(PO_4)_2$ (33), $Na_2(Fe_{0.5}^{3+}Fe_{0.5}^{2+})_2Fe^{2+}(PO_4)_3$ (34), $KFeFPO_4$ (35), and $KFe_4(PO_4)_3$ (9), there is

© 2006 NRC Canada

Fig. 4. (A) Size distribution for particles synthesized with τ = 120 min, vol(HCl):vol(Co) = 2:5, and temperature equal to (*a*) 400 °C and (*b*) 450 °C; (B) size distribution for particles synthesized at 400 °C with τ = 120 min and ratio vol(HCl):vol(Co) = (*a*) 3:5 and (*b*) 2:5; (C) size distribution for particles synthesized at 400 °C with ratio vol(HCl):vol(Co) = 3:5, after (*a*) 0 min, (*b*) 10 min, and (*c*) 120 min.

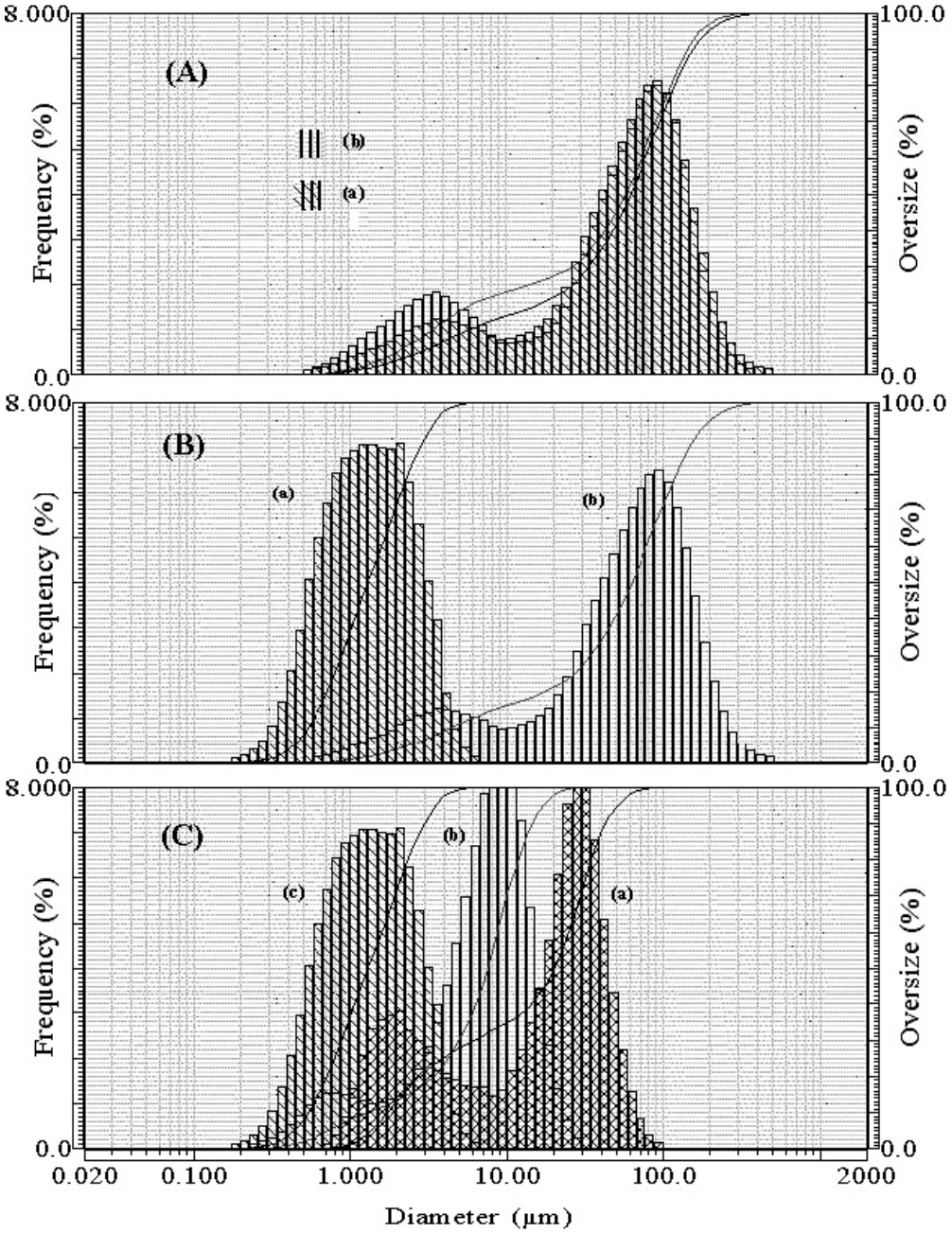

typically at least one unit cell constant that is approximately equal to six or to multiples of this value. The pertinent parameter in our case, c = 6.2004, determines the lattice spacing along the c axis of the unit cell. This value is due to chains of alternating [FeO_6] octahedra and [PO_4^{3-}] tetrahedra, linked by their vertices (Fig. 6*b*).

Vibrational spectra

The new orthophosphate salt, $KCo_3Fe(PO_4)_3$, crystallizes in the orthorhombic space group *Pnnm* (D_{2h}^{12}) with Z = 4. The P atoms lie on C_s sites. The proposed vibrational band assignments for the IR and Raman spectra of the salt are given in Table 5. The absence of the symmetric stretching and antisymmetric H–O(P) bending vibrations at ~2300 and ~1447 cm^{-1}, respectively, confirms that the salt does not contains H atoms. The nature of the four normal vibrations (ν_1, ν_2, ν_3, and ν_4 in Herzberg notation (36)) of the PO_4^{3-} groups was determined by the site group method of Halford (37), in which the normal modes of the free ion are correlated to the vibrations in the site and crystal symmetry.

© 2006 NRC Canada

Table 5. Proposed vibrational band assignments for $KCo_3Fe(PO_4)_3$ (cm^{-1}).

IR	Raman	Assignment	
	1070	A_g+B_g	$\nu_{asym}PO$
1067		$B_{1u}+B_2u+B_{3u}$	
	1039	A_g+B_g	
980		B_{1u}	$\nu_{sym}PO$
	970	A_g	
920		B_{1u}	
	915	B_{1g}	
629	608	$B_{1u}+B_2u+B_{3u}$	$\delta_{asym}PO_2$
587	560sh		
533			
520	470sh		
439		$B_{1u}+B_2u+B_{3u}$	
	390	$A_g+B_{1g}+B_{2g}+B_{3g}$	$\delta_{sym}PO_2$
380	300		External modes
365	235		
355	205		
	180		

Theoretically, each vibrational mode of the PO_4^{3-} ions could be split into four components by dynamic coupling between the four anions in the primitive unit cell. The full influence of the site and factor groups on the internal vibrations of the PO_4^{3-} ions is, however, not observed for each mode. If the vibrations of the three different PO_4^{3-} groups were equivalent, only one vibration would be expected in both the IR and Raman spectra under the influence of the site effect. If the factor group effect is predominating, there should be two Raman bands and one IR band observed. However, two bands were observed in the Raman spectrum and another two bands in the IR spectrum, thereby confirming that the PO_4^{3-} groups are indeed different, in agreement with the crystallographic results. Finally, most of the IR bands are noncoincident with those observed in the Raman spectrum, in accord with the centrosymmetric nature of the crystal.

The Raman spectra of the amorphous powders obtained under different SCW conditions indicate the presence of orthophosphate groups, and as expected for amorphous materials, the spectra are characterized by weak, extremely broad bands and a relatively high and featureless background. The bands observed at ~1000 cm^{-1} correspond to the A_g symmetric P–O stretching mode.

Vibrational spectroscopy often plays a prominent role in the structural study of inorganic crystals, especially in cases where X-ray diffraction fails to give unequivocal results, such as for glasses and amorphous materials. The correlation between X-ray diffraction results and vibrational spectroscopy has become of practical importance. A linear empirical correlation was established recently (38) for inorganic crystalline phosphates between the wavenumbers of the Raman-active P–O stretching modes and the associated P—O bond lengths. This correlation has been tested and extended with success to glassy and amorphous phosphate materials, such as $Na_5Ti(PO_4)_3$ glass (39). The unpolarized vibrational spectra of crystals and their amorphous or glassy analogues are often quite similar because the vibrational spectra are determined largely by short-range order. There are two established empirical equations used nowadays (38) to calculate P—O bond lengths (in pm), as follows:

Fig. 5. ORTEP view of asymmetric unit with atomic numbering scheme (ellipsoids drawn at 60% probability level). Symmetry codes ^{I}: x, y, $-z$, ^{II}: $-x+1$, $-y+1$, $-z$, ^{III}: $x-1/2$, $-y+1/2$, $-z-1/2$, ^{IV}: $x-1/2$, $-y+1/2$, $z+1/2$, ^{V}: $x-1/2$, $-y+1/2$, $z-1/2$, ^{VI}: $-x+1/2$, $y-1/2$, $z-1/2$, ^{VII}: $-x+1/2$, $y-1/2$, $-z+1/2$, ^{VIII}: $x+1/2$, $-y+1/2$, $z+1/2$, ^{IX}: $x+1/2$, $-y+1/2$, $z-1/2$, ^{X}: $-x+1/2$, $y-1/2$, $-z-1/2$, ^{XI}: $-x$, $-y+1$, $-z$.

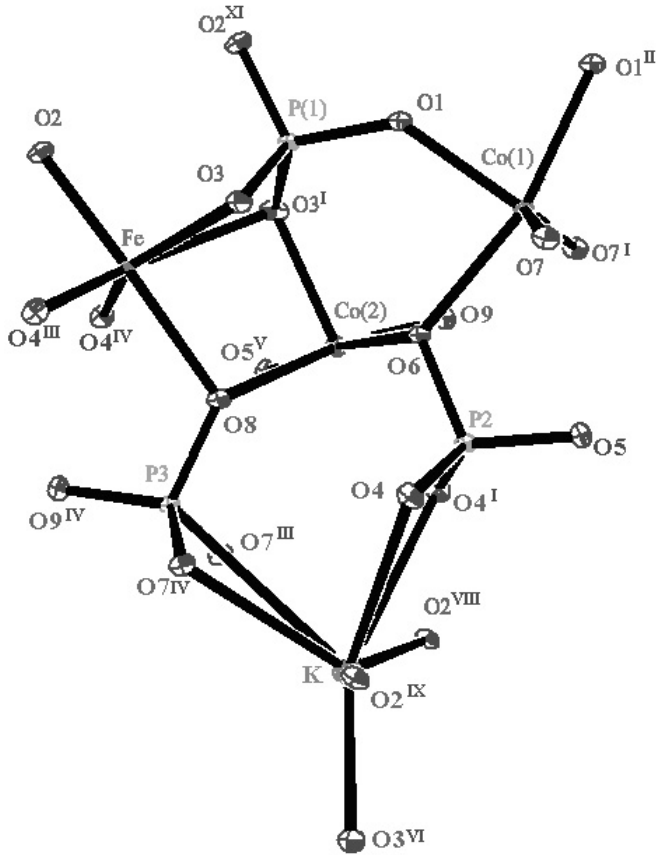

[1] $\nu = 6.3 \times 10^3 - 34.3R$

[2] $\nu_w = 224\,500 \exp(-R/28.35)$

These two equations were used in our case to predict the P—O bond lengths in the amorphous orthophosphates obtained under different SCW experimental conditions. The results agree well with the values found for other orthophosphates (Table 6). The precision in the estimation of a P—O bond length from a measured Raman wavenumber using the bond length – stretching wavenumber correlation is 1 pm. The standard deviation in the estimate of a Raman stretching wavenumber from an absolute P—O bond length is 37 cm^{-1}. The observed Raman bands exhibited slight shifts, but noticeably broadened and decreased in intensity, with the increasing SCW reaction time. For the experiment run at 450 °C for 120 min, a new phase was produced (Fig. 7*d*), which is different from those obtained previously (Fig. 7*a*–7*c*), and this material has yet to be identified.

© 2006 NRC Canada

Table 6. Raman stretching wavenumbers for P—O bonds in amorphous orthophosphate powders obtained under SCW conditions and the predicted P—O bond lengths from eqs. [1] and [2].

Reaction conditions	Stretching wavenumbers	P—O bond lengths from eq. [1] (Å)	P—O bond lengths from eq. [2] (Å)
450 °C, 120 min	998 νs	1.546	1.535
	1060 νas	1.527	1.518
450 °C, 30 min	1040 νs	1.533	1.524
450 °C, 10 min	1005 νs	1.544	1.533
	1045 νs	1.532	1.522

Note: Equations [1] and [2] predict the bond lengths in picometers. These values have been converted to angstroms (100 pm = 1 Å) for more ready comparison with the X-ray results. For stretching wavenumbers, s is symmetric frequency and as is asymmetric frequency.

Fig. 6. Three-dimensional view of the structure of $KCo_3Fe(PO_4)_3$ viewed down the (*a*) *c* axis; (*b*) *b* axis; and (*c*) *a* axis (program Molview).

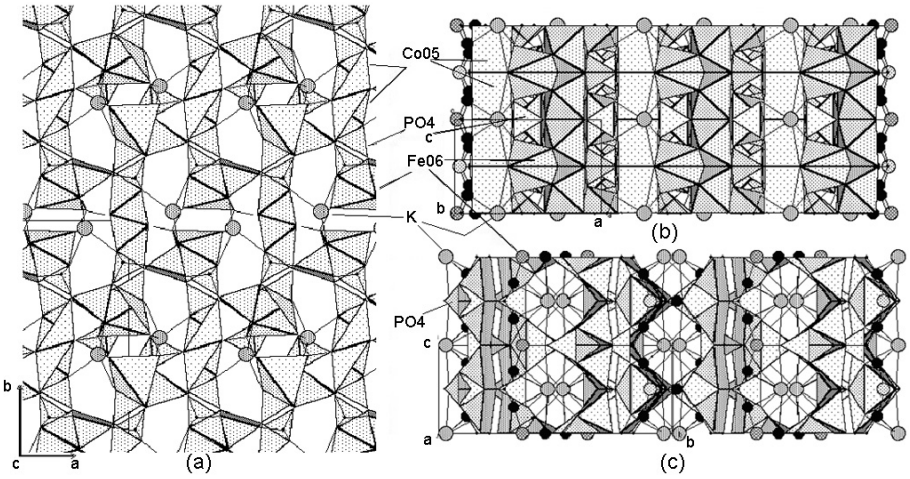

Fig. 7. Raman spectra of powder obtained after reaction under different SCW conditions: (*a*) 450 °C, 120 min; (*b*) 450 °C, 30 min; (*c*) 450 °C, 10 min; and (*d*) 450 °C, 120 min (an extra phase).

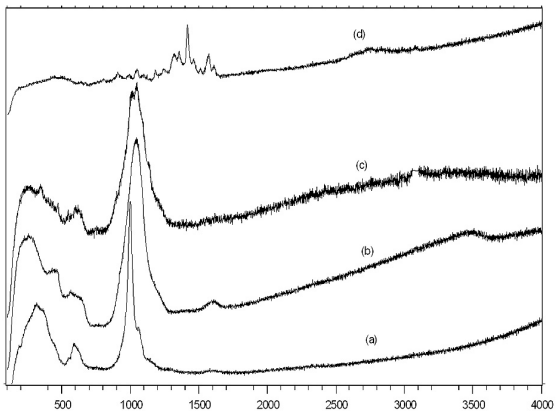

Acknowledgements

This research was supported by operating and equipment grants from the Natural Sciences and Engineering Research Council of Canada (NSERC) and Le fonds québécois de la recherche sur la nature et les technologies (FQRNT).

References

1. G.W. Morey and P. Niggli. J. Am. Chem. Soc. **35**, 1086 (1913).
2. A. Rabenau. Angew. Chem. Int. Ed. Engl. **24**, 1026 (1986).
3. T. Adschiri, K. Kanazawa, and K. Arai. J. Am. Ceram. Soc. **75**, 2615 (1992).
4. J.A. Darr and M. Poliakoff. Chem. Rev. **99**, 495 (1999).
5. A. Cabanas, J.A. Darr, T. Ilkenhans, and M. Poliakoff. In Proceedings of 6th meeting on supercritical fluids. *Edited by* M. Poliakoff. Chemistry and Materials, Nottingham, England. 1999.
6. J. Lee and A.S. Teja. Supercrit. Fluids. **35**, 83 (2005).
7. D.E.C. Corbridge. Bull. Soc. Fr. Mineral. Cristallogr. **94**, 271 (1971).
8. S. Apinitis. Latv. Kim. Z. **6**, 664 (1991).
9. E.N. Matvienko, O.V. Yakubovich, M.A Simonov, and N.V. Belov. Dokl. Akad. Nauk SSSR, **259(3)**, 591 (1981).
10. M. Pintard-Screpel, F. D'Yvoire, and J. Durand. Acta Cryst. **C39**, 9 (1983).
11. S. Neeraj, M.L. Noy, C.N.R. Rao, and A.K. Cheetham. J. Solid State Chem. **167**, 344 (2002).
12. K.-H. Lii and Y.-F. Huang. Chem. Commun. **9**, 839 (1997).
13. J.M. Thomas, R. Raja, G. Sankar, and R.G. Bell. Nature (London), **398**, 227 (1999).
14. J. Chen and J.M. Thomas. J. Chem. Soc. Chem. Commun. 603 (1994).
15. J.M. Thomas and W.J. Thomas. Principles and practice of heterogeneous catalysis. VCH verlagsgesellschart mbH, Weinheim, Germany. 1997.

© 2006 NRC Canada

16. P.A. Barrett, R.H. Jones, J.M. Thomas, G. Sankar, I.J. Shannon, and C.R.A. Catlow. J. Chem. Soc. Chem. Commun. 2001 (1996).
17. W.A. Bassett, A.H. Shen, M. Bucknum, and I.-M. Chou. Rev. Sci. Instrum. **64**, 2340 (1993).
18. F. Capitelli, M. Harcharras, H. Assaaoudi, A. Ennaciri, A.G.G. Moliterni, and V. Bertolasi. Z. Kristallogr. **218**, 345 (2003).
19. G.M. Sheldrick. SHELXS97 [computer program]. University of Göttingen, Göttingen, Germany. 1997.
20. G.M. Sheldrick. SHELXL97 [computer program]. University of Göttingen, Göttingen, Germany. 1997.
21. M.N. Burnett and C.K. Johnson. ORTEP-III [computer program]. Oak Ridge National Laboratory Report ORNL-6895, Oak Ridge, Tenn. 1996.
22. L.J. Farrugia. J. Appl. Crystallogr. **30**, 565 (1997).
23. T.J. Smith. J. Mol. Graphics, **13**, 122 (1995).
24. D.P.E. Dickson and F.J. Berry. Mossbauer spectroscopy. Cambridge University Press, New York. 1986.
25. D. Kobashi, S. Kohara, J. Yamakawa, and A. Kawahara. Acta Crystallogr. **C53**, 1523 (1997).
26. Y. Dumas, J.L. Galigne, and J. Falgueirettes. Acta Crystallogr. **B29**, 1623 (1973).
27. R.D. Shannon. Acta Crystallogr. **A32**, 751 (1976).
28. O.V. Yakubovich, M.S. Dadashov, and B.N. Litvin. Sov. Phys. Crystallogr. **33**, 16 (1988).
29. Y. Dumas, J. Lapasset, and J. Vicat. Acta Crystallogr. **B36**, 2754 (1980).
30. A.A. Tahiri, R. Oursanal, M. Lachnar, B. El Bali, and M. Bolte. Acta Crystallogr. **E58**, 91 (2002).
31. O.V. Yakubovich, M.A. Simonov, and N.V. Belov. Sov. Phys. Dokl. **22**, 347 (1977)
32. O.V. Yakubovich, M.A. Simonov, E.N. Matvienko, and N.V. Belov. Sov. Phys. Dokl. **23**, 11 (1978); Dokl. Akad. Nauk SSSR, **238**(3), 576 (1978).
33. K. Yu, M.A. Kabalov, O.V. Simonov, N.A. Yakubovich, N.V. Yamnova, and N.A. Belov. Sov. Phys. Dokl. **18**, 362 (1973); Dokl. Akad. Nauk SSSR, **210**, 830 (1973).
34. O.V. Yakubovich, M.A. Simonov, K. Yu, N. Egorov-Tismenko, and N.V. Belov. Sov. Phys. Dokl. **22**, 570 (1977); Dokl. Akad. Nauk SSSR, **236**, 1123 (1977).
35. E.N. Matvienko, O.V. Yakubovich, M.A. Simonov, and N.V. Belov. Sov. Phys. Dokl. **24**, 411 (1979); Dokl. Akad. Nauk SSSR, **246**, 875 (1979).
36. G. Herzberg. Infrared and raman spectra of polyatomic molecules. Van Nostrand, Princeton, New Jersey. 1946.
37. R.S. Halford. J. Chem. Phys. **14**, 8 (1946).
38. L. Popovic, D. de Waal, and J.C.A. Boeyens. J. Raman Spectrosc. **36**, 2 (2005).
39. S. Krimi, A. El Jazouli, L. Rabardel, M. Couzi, I. Mansouri, and G. Le Flem. J. Solid State Chem. **102**, 400 (1993).

© 2006 NRC Canada